



Engineering FeOOH/Ni(OH)₂ heterostructures on Ni₃S₂ surface to enhance seawater splitting

Chen Yang, Ya-Dong Li, Li-Juan Cao, Xi-Long Wang, Han-Pu Liang* 

Received: 8 May 2023 / Revised: 20 July 2023 / Accepted: 21 July 2023 / Published online: 3 February 2024
© Youke Publishing Co., Ltd. 2024

Abstract The construction of highly stable and efficient electrocatalysts is desirable for seawater splitting but remains challenging due to the high concentration of Cl⁻ in seawater. Herein, FeOOH/Ni(OH)₂ heterostructure supported on Ni₃S₂-covered nickel foam (Fe–Ni/Ni₃S₂/NF) was fabricated by hydrothermal and etching methods, as well as anodic oxidation process. The electronic structure of FeOOH and Ni(OH)₂ could be modulated after depositing FeOOH nanoparticles on Ni(OH)₂ nanosheet, which greatly boosted the catalytic activity. When the catalyst used as an electrode for oxygen evolution reaction (OER), it needed low overpotentials of 266 and 368 mV to achieve current densities of 100 and 800 mA·cm⁻², respectively, in 1 mol·L⁻¹ KOH + seawater electrolyte. It can operate continuously at 100 mA·cm⁻² for 400 h without obvious decay. Particularly, in situ generated SO₄²⁻ from inner Ni₃S₂ during electrolysis process would accumulate on the surface of active sites to form

passivation layers to repel Cl⁻, which seemed to be responsible for superior stability. The study not only synthesizes an OER catalyst for highly selective and stable seawater splitting, but also gives a novel approach for industrial hydrogen production.

Keywords Anodic oxidation; Heterostructure; Oxygen evolution reaction; Seawater splitting

1 Introduction

Water electrolysis for hydrogen production is regarded as a sustainable energy-conversion technology, attracting significant global interest [1–4]. Most electrocatalytic devices currently in use operate at different pH levels in freshwater electrolyte [5–9]. However, extensive use of freshwater electrolysis would deplete freshwater resources. Due to the abundance of seawater on Earth, producing hydrogen from seawater is more favorable than that from freshwater [10]. Nonetheless, seawater electrolysis has a lot of challenges to overcome, including competitive chlorine evolution reaction (CER) and severe Cl⁻ corrosion [11–13].

The key challenge of seawater electrolysis is the CER process that competes with oxygen evolution reaction (OER) on anode under high chlorine concentration (~ 0.5 mol·L⁻¹) in seawater [14, 15]. When the pH value of the electrolyte exceeds 7.5, the potential difference between CER and OER reaches a maximum of 480 mV [16]. Thus, to achieve 100% OER efficiency during seawater splitting, the overpotentials must be less than 480 mV. Additionally, CER process should also be avoided under large current densities for industrial application, which requires the ideal catalysts to have high activity.

Chen Yang and Ya-Dong Li have contributed equally to this work.

Supplementary Information The online version contains supplementary material available at <https://doi.org/10.1007/s12598-023-02590-9>.

C. Yang, Y.-D. Li, L.-J. Cao, X.-L. Wang, H.-P. Liang*
Qingdao Institute of Bioenergy and Bioprocess Technology,
Chinese Academy of Sciences, Qingdao 266101, China
e-mail: lianghp@qibebt.ac.cn

C. Yang, H.-P. Liang
Center of Materials Science and Optoelectronics Engineering,
University of Chinese Academy of Sciences, Beijing 100049,
China

Y.-D. Li, L.-J. Cao
Sino-Danish College, University of Chinese Academy of
Sciences, Beijing 100049, China



Although there are a few studies on OER catalysts for seawater splitting, the activity and selectivity of the catalysts need further improvement [17–19]. Fortunately, the construction of heterostructures has been confirmed as an effective strategy to enhance OER activity and selectivity in alkaline seawater electrolyte by exposing more active sites [20–24].

Severe Cl^- corrosion poses another challenge in seawater electrolysis [25–30]. However, our previous findings suggested that PO_4^{3-} formed on the surface of catalysts could effectively repel Cl^- and enhance corrosion resistance during seawater splitting [31]. Similarly, Kuang et al. [14] reported that a SO_4^{2-} -rich passivation layer could improve the corrosion resistance of the anode by repelling Cl^- . Both reports indicate that constructing an anion-rich layer on the surface of active sites is an effective approach to mitigate Cl^- corrosion during seawater electrolysis.

To address these two major challenges, a Fe–Ni/Ni₃S₂/NF electrode with high corrosion resistance was fabricated, where FeOOH nanoparticles were uniformly deposited on Ni(OH)₂ nanosheets. The resulting FeOOH/Ni(OH)₂ heterostructures provide abundant active sites, conferring superior electrocatalytic performance to the electrode during alkaline seawater splitting. The Fe–Ni/Ni₃S₂/NF showed a low overpotential of 247 mV at 100 mA·cm^{−2} in 1 mol·L^{−1} KOH. Moreover, it maintained superior activity even in alkaline natural seawater electrolyte, requiring an overpotential of 266 mV at 100 mA·cm^{−2}. By coupling this anode with the previously reported cathode, the two-electrode electrolyzer required a low voltage of 1.69 V at a current density of 100 mA·cm^{−2} in alkaline seawater. Besides, the electrolyzer exhibited high stability with minimal degradation over 400 h of operation. Impressively, SO_4^{2-} -rich passivation layers generated from the oxidation of inner Ni₃S₂ seem to be responsible for the superior stability in seawater electrolyte.

2 Experimental

2.1 Preparation of catalysts

2.1.1 Synthesis of Ni/Ni₃S₂/NF electrode

A homogeneous solution was prepared by dissolving 14.4 g Na₂S·9H₂O in 50 ml deionized (DI) water. The solution and clean nickel foam (NF) substrate were then placed to a 100 ml Teflon-lined stainless-steel autoclave and heated at 170 °C for 10 h. After being cooled to room temperature and repeatedly being washed with DI water, the Ni₃S₂/NF sample was obtained. The Ni₃S₂/NF electrode was then

immersed in a 28 mmol·L^{−1} Ni(NO₃)₂·6H₂O solution for 4 h to create Ni/Ni₃S₂/NF electrode.

2.1.2 Synthesis of Fe–Ni/Ni₃S₂/NF, Fe/Ni₃S₂/NF, and Ni p/Ni₃S₂/NF electrodes

Fe–Ni/Ni₃S₂/NF electrode was prepared through an anodic oxidation process. In detail, the graphite and Ni/Ni₃S₂/NF electrodes were employed as counter and working electrodes, respectively. Two-electrode electrolyzer was conducted in 0.01 mol·L^{−1} (NH₄)₂Fe₂(SO₄)₂ solution at 1.2 mA·cm^{−2} for 15 min to obtain Fe–Ni/Ni₃S₂/NF electrode.

Fe/Ni₃S₂/NF and Ni p/Ni₃S₂/NF electrodes were prepared by using the same method as Fe–Ni/Ni₃S₂/NF. However, during the preparation of Fe/Ni₃S₂/NF electrode, Ni₃S₂/NF was used as the working electrode in the anodic oxidation process. For Ni p/Ni₃S₂/NF electrode, (NH₄)₂SO₄ solution was used instead of (NH₄)₂Fe₂(SO₄)₂.

2.1.3 Synthesis of Fe–Ni/NF electrode

A hydrothermal process was used to produce Ni/NF. To make a homogeneous solution, 582 mg of Ni(NO₃)₂·6H₂O, 600 mg of urea, and 148 mg of NH₄F were dissolved in 40 ml of DI water. The solution and the clean NF substrate were then placed in a 100 ml Teflon-lined stainless-steel autoclave and heated at 120 °C for 10 h. After cooling and washing, the Ni/NF sample was obtained. Fe–Ni/NF electrode was made using the same anodic oxidation procedure as the Fe–Ni/Ni₃S₂/NF electrode, but Ni/NF was used instead of Ni/Ni₃S₂/NF.

2.2 Electrochemical characterization

The electrochemical performance was evaluated on an electrochemical station (CHI 660E). The as-prepared electrode, Pt mesh, and standard Hg/HgO electrode were employed as working electrode, counter electrode, and reference electrode, respectively. OER was performed at 25 °C in a three-electrode setup. If not otherwise stated, the potentials were calibrated to the reversible hydrogen electrode (RHE) with 85% iR-compensation.

OER polarization curve was measured at a scan rate of 2 mV·s^{−1}. Electrochemical impedance spectroscopy (EIS) was recorded at 1.5 V from 0.1 Hz to 100 kHz with an amplitude of 10 mV. Cyclic voltammetry (CV) was used to measure the double-layer capacitance (C_{dl}) in the non-faradaic zone.

Two-electrode electrolyzer was assembled by coupling Fe–Ni/Ni₃S₂/NF electrode with the previously obtained P-NiMoO electrode [31].

3 Results and discussion

Synthesis process for the heterogeneous Fe–Ni/Ni₃S₂/NF electrode is depicted in Fig. 1. Firstly, the hydrothermal sulfidation method was deployed to synthesize Ni₃S₂ on the surface of NF using bare NF as the matrix and Ni source. Scanning electron microscopy (SEM) images in Fig. S1a, b show that after sulfidation, the NF surface exhibits protrusions in the form of peak-like structures. High-resolution transmission electron microscopy (HRTEM) analysis (Fig. S1c) identifies the Ni₃S₂ with lattice *d*-spacings of 0.409 and 0.285 nm, corresponding to the (101) and (110) planes, respectively. Selected area electron diffraction (SAED) pattern in Fig. S1d confirms that the material is Ni₃S₂. Subsequently, etching in Ni(NO₃)₂ solution, as shown in Fig. S2, covers the surface of the as-prepared Ni₃S₂/NF with Ni(OH)₂ nanoflowers, which are generated uniformly and vertically on the Ni₃S₂ surface. Finally, FeOOH nanoparticles are deposited on Ni(OH)₂ nanosheets after an anodic oxidation process. Figures 2a–c, S3 show that Fe–Ni/Ni₃S₂/NF electrode retains its nanoflower morphology without any damage.

Typical X-ray diffraction (XRD) patterns in Fig. S4 show three distinct peaks, which are indexed to the nickel foam substrate. The additional peaks in the patterns are assigned to Ni₃S₂ (PDF No. 44-1418), indicating successful synthesis of Ni₃S₂ arrays after the sulfidation procedure. However, XRD patterns of Ni/Ni₃S₂/NF and Fe–Ni/Ni₃S₂/NF do not show diffraction peaks of Ni(OH)₂ and FeOOH, possibly due to their poor crystallinity. Figure 2d, e shows high-angle annular dark-field scanning transmission electron microscopy (HAADF-STEM) and transmission electron microscopy (TEM) images of Fe–Ni/Ni₃S₂, confirming the nanoflower morphology composed of interlaced nanosheets. HRTEM images in Fig. 2f demonstrate the homogeneous distribution of FeOOH nanoparticles with a size of ~ 2 nm after anodic oxidation process. According to Figure. S5, it provides evidence in the opposite direction for the formation of FeOOH. The low crystallinity of FeOOH and Ni(OH)₂ phases is further revealed by the indistinct diffraction rings in SAED pattern (Fig. 2g), which is consistent with XRD results [32].

Energy-dispersive X-ray spectrometer (EDX) mapping images in Fig. 2h–l show the uniform distribution of Fe, Ni, S and O elements in FeOOH/Ni(OH)₂ heterostructures. Figure S6 displays the corresponding elemental composition of Fe–Ni/Ni₃S₂/NF electrode. Notably, S element is uniformly distributed in the nanoflowers, except for the brilliant spots caused by Ni₃S₂ residue during scraping in Fig. 2k. This suggests that SO₄^{2–} produced by Ni₃S₂ during anodic oxidation may accumulate on the surface of active sites.

X-ray photoelectron spectroscopy (XPS) was further employed to examine the valence and surface chemical composition of the prepared electrocatalysts. XPS survey of the Fe–Ni/Ni₃S₂/NF electrode (Fig. S7) clearly shows peaks corresponding to Fe, Ni, S and O elements, which is consistent with the element mapping results. In the Ni 2p XPS spectra (Fig. 3a), the two peaks at the binding energies of 852.6 and 869.9 eV are attributed to the Ni 2p_{3/2} and Ni 2p_{1/2} of Ni⁰⁺ in nickel sulfide, respectively [33, 34]. The binding energies of 855.7 and 873.3 eV are assigned to the Ni 2p_{3/2} and Ni 2p_{1/2} of Ni²⁺ for Ni(OH)₂, respectively [35, 36]. Specifically, the binding energy of Ni 2p_{3/2} is positively shifted after the formation of FeOOH nanoparticles, indicating the modulation of electronic structure. Figure S8 vividly demonstrates the electron transfer from Ni(OH)₂ to FeOOH, which optimizes the adsorption of oxygen evolution reaction OER intermediates, ultimately resulting in improved catalytic performance [37]. The absence of Ni³⁺ peaks in the Ni 2p spectra indicates the absence of NiOOH formation during the anodic oxidation process. To further demonstrate the absence of NiOOH, a comparative electrode of Ni p/Ni₃S₂/NF was also prepared, which followed a similar sample preparation method as Fe–Ni/Ni₃S₂/NF, using a similar sample preparation method to Fe–Ni/Ni₃S₂/NF, with the exception of using (NH₄)₂SO₄ instead of (NH₄)₂Fe(SO₄)₂ during the anodic oxidation process. Figure S9 shows the XPS results of Ni p/Ni₃S₂/NF. Ni 2p spectrum reveals the presence of Ni in the 2+ state, while the O 1s spectrum lacks a peak corresponding to Ni–O bonds, indicating the formation of Ni(OH)₂ instead of NiOOH. As shown in Fig. 3b of Fe 2p XPS spectrum, the binding energies of 711.5 and 725.0 eV

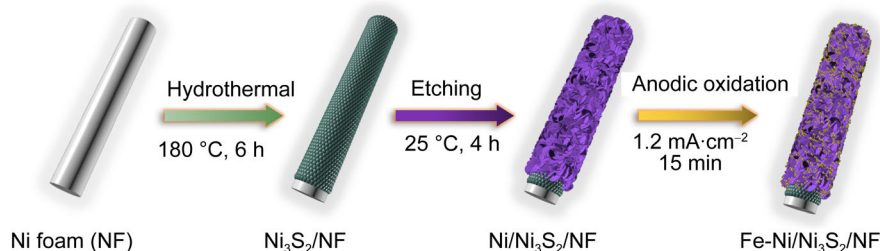


Fig. 1 Illustration of synthesis of Fe–Ni/Ni₃S₂/NF electrode

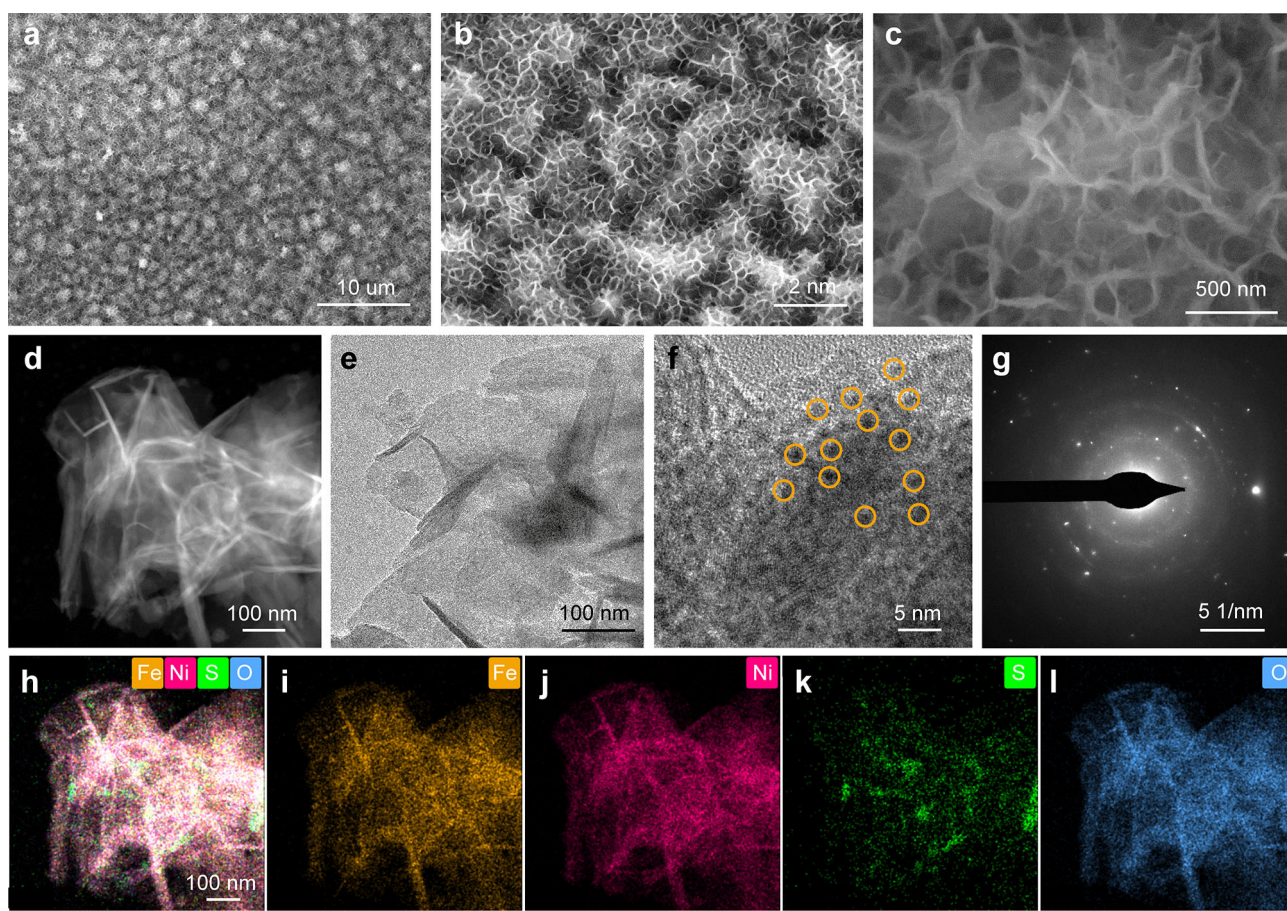


Fig. 2 a–c SEM images of Fe–Ni/Ni₃S₂/NF electrode; d HAADF-STEM, e TEM and f HRTEM images of Fe–Ni/Ni₃S₂ electrocatalyst scrapped from as-prepared electrode; g corresponding electron diffraction pattern and h–l EDX mappings of Fe–Ni/Ni₃S₂ electrocatalyst

are ascribed to the Fe 2p_{3/2} and Fe 2p_{1/2} of Fe³⁺, respectively [38]. In particular, the peak at the binding energy of 705.2 eV is attributed to Ni auger [31, 39]. Figure 3c shows the O 1s XPS spectra, and the wide peak can be separated into three peaks at 529.4, 531.0 and 532.1 eV, which correspond to the peaks of M–O, M–OH and adsorbed H₂O, respectively [37]. Combining with the results of Fig. S9b, it is clear that M–O in Fig. 3c belongs to FeOOH rather than NiOOH. The S 2p spectra of Fe–Ni/Ni₃S₂/NF and Ni/Ni₃S₂/NF electrodes are exhibited in Fig. 3d. The first doublet of S 2p_{3/2} and S 2p_{1/2} at about 162.9 and 164.1 eV is attributed to S₂²⁻ [40, 41]. The other doublet at about 161.9 and 163.3 eV corresponds to S²⁻, indicating the formation of a small amount of NiS during the sulfidation process [40, 42]. Furthermore, for Fe–Ni/Ni₃S₂/NF electrode, the peak at 168.7 eV can be ascribed to SO₄²⁻, which is formed during the anodic oxidation process from nickel sulphide [14]. To further demonstrate the formation of SO₄²⁻, an analysis on the reference sample was conducted. From the S 2p spectra shown in Fig. S9c, it can be observed that the Ni/Ni₃S₂/NF electrode, after undergoing

anodic oxidation in (NH₄)₂SO₄, also exhibits a peak at a binding energy of 168.9 eV, indicating the presence of S–O bonds. This provides further evidence to suggest that the anodic oxidation process promotes the formation of SO₄²⁻.

OER performances of Fe–Ni/Ni₃S₂/NF catalysts, Ni/Ni₃S₂/NF, NF and commercial IrO₂ were investigated in 1 mol·L⁻¹ KOH at 25 °C. Figure 4a reveals that Fe–Ni/Ni₃S₂/NF electrode exhibits a considerable improvement in OER when compared to Ni/Ni₃S₂/NF, NF and commercial IrO₂. Figure 4b summarizes the overpotentials at different current densities of 100, 200, 400, 800 and 1,000 mA·cm⁻² for Fe–Ni/Ni₃S₂/NF and Ni/Ni₃S₂/NF electrodes in 1 mol·L⁻¹ KOH. Specifically, at current densities of 100, 400 and 800 mA·cm⁻², Fe–Ni/Ni₃S₂/NF electrode requires overpotentials of 247, 278 and 297 mV, respectively. After the deposition of FeOOH by anodic oxidation, the overpotential of Fe–Ni/Ni₃S₂/NF is much lower than that of Ni/Ni₃S₂/NF at various current densities. According to Fig. 4c, the overpotential of Fe–Ni/Ni₃S₂/NF at 100 mA·cm⁻² is also lower than that of most of the non-noble metal based self-supported OER electrocatalysts

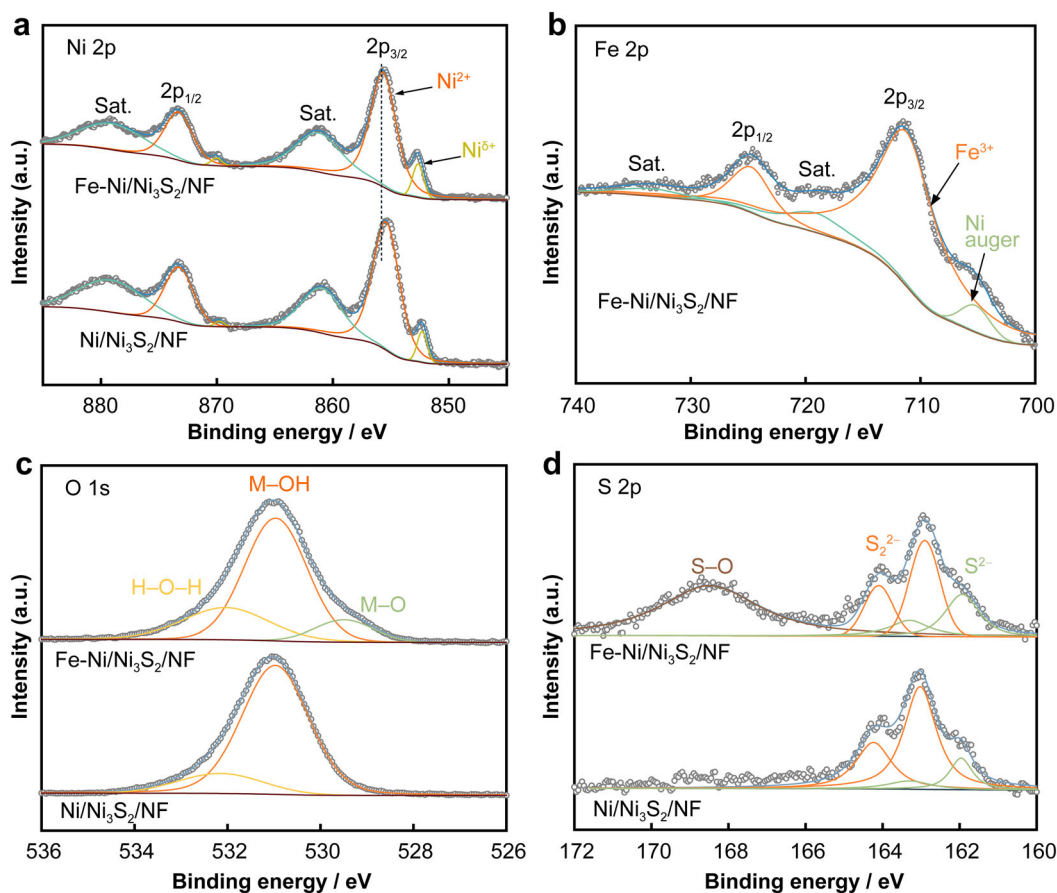


Fig. 3 High-resolution XPS spectra of **a** Ni 2p, **b** Fe 2p, **c** O 1s and **d** S 2p for Fe–Ni/Ni₃S₂/NF and Ni/Ni₃S₂/NF electrodes

(Table S1). In addition, we also prepared an Fe/Ni₃S₂/NF electrode for comparison, and its polarization curve is shown in Fig. S10. When the current density reaches 100 mA·cm⁻², the required overpotential is 274 mV, which is higher than that of the Fe–Ni/Ni₃S₂/NF electrode. This indicates that the construction of FeOOH/Ni(OH)₂ heterostructure greatly enhances the performance.

Figure 4d reveals that Fe–Ni/Ni₃S₂/NF electrode shows a lower Tafel slope (52.9 mV·dec⁻¹) compared to Ni/Ni₃S₂/NF (106.5 mV·dec⁻¹), and NF (191.7 mV·dec⁻¹), indicating faster electrocatalytic kinetics. EIS in Fig. 4e demonstrates that Fe–Ni/Ni₃S₂/NF electrode has a low charge-transfer resistance (R_{ct}) of 0.22 Ω , which is lower than that of Ni/Ni₃S₂/NF (0.70 Ω) and NF (2.61 Ω), signifying superior electronic conductivity and charge transfer. The C_{dl} values obtained from the CV curves in Fig. S11 are presented in Fig. 4f. The C_{dl} values of the Fe–Ni/Ni₃S₂/NF, Ni/Ni₃S₂/NF and NF electrodes are 6.8, 37 and 43 mF·cm⁻², respectively, implying that the formed FeOOH/Ni(OH)₂ heterostructure has a larger electrochemical surface area and more abundant active sites. Fe–Ni/Ni₃S₂/NF electrode also exhibits a hydrophilic characteristic (Fig. S12), facilitating electrolyte transport and

rapid release of gas bubbles. This is a key factor contributing to the significantly enhanced OER activity of the Fe–Ni/Ni₃S₂/NF electrode, especially at high current densities [20, 43].

Another crucial criterion is stability, which is evaluated by chronopotentiometric and CV measurements in 1 mol·L⁻¹ KOH at 25 °C. As shown in Fig. 4g, the overpotential at 100 mA·cm⁻² increases by only 7 mV after 5000 CV scans. According to chronopotentiometric curve for the Fe–Ni/Ni₃S₂/NF electrode at a current density of 100 mA·cm⁻² shown in Fig. 4h, the electrochemical catalytic activity remains stable over 80 h without noticeable decline. These findings suggest that the Fe–Ni/Ni₃S₂/NF electrode is highly durable during OER process.

The activity of the Fe–Ni/Ni₃S₂/NF electrode was evaluated for OER in alkaline simulated seawater (1 mol·L⁻¹ KOH + 0.5 mol·L⁻¹ NaCl) and alkaline natural seawater (1 mol·L⁻¹ KOH + seawater). In the 1 mol·L⁻¹ KOH + 0.5 mol·L⁻¹ NaCl electrolyte, as presented in Fig. 5a, the Fe–Ni/Ni₃S₂/NF electrode exhibits excellent activity and needs overpotentials of 266, 306 and 334 mV to achieve current densities of 100, 400 and 800 mA·cm⁻², respectively (Fig. 5b). Even in 1 mol·L⁻¹

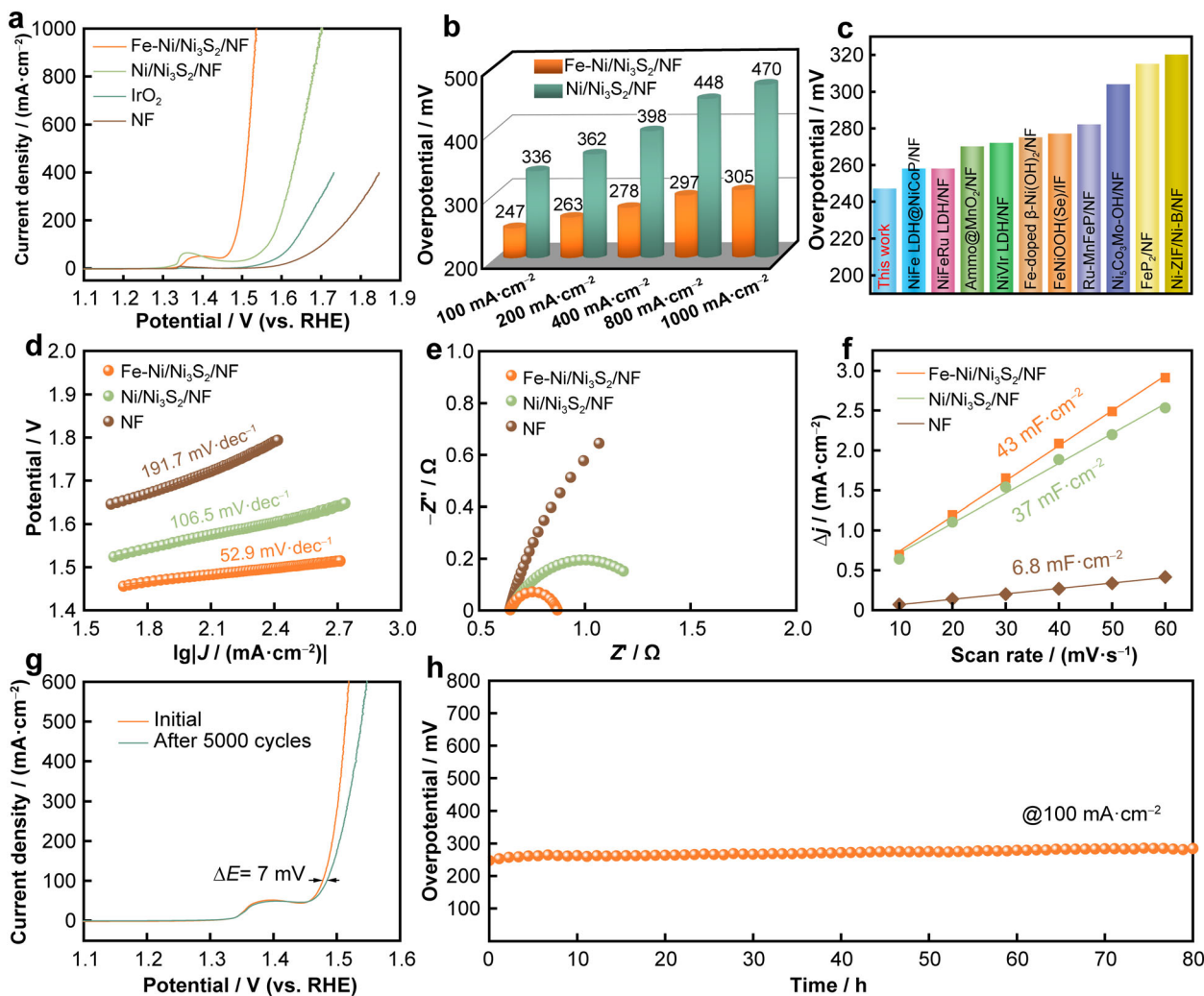


Fig. 4 **a** Polarization curves of Fe–Ni/Ni₃S₂/NF, Ni/Ni₃S₂/NF, NF and commercial IrO₂ for OER in 1 mol·L⁻¹ KOH; **b** comparison of overpotentials required to achieve current densities of 100, 200, 400, 800 and 1000 mA·cm⁻²; **c** comparison of OER activity for Fe–Ni/Ni₃S₂/NF electrode with other recently reported OER electrocatalysts at 100 mA·cm⁻²; corresponding **d** Tafel plots, **e** EIS and **f** C_{dl} data of prepared electrodes; **g** polarization curves of Fe–Ni/Ni₃S₂/NF electrode before and after 5000 cycles; **h** chronopotentiometric curve of Fe–Ni/Ni₃S₂/NF electrode at a current density of 100 mA·cm⁻² in 1 mol·L⁻¹ KOH

KOH + seawater, the required overpotentials at current densities of 100, 400 and 800 mA·cm⁻² are 266, 326 and 368 mV, respectively. The overpotentials at high current densities are significantly lower than 480 mV, which indicates the high OER selectivity in seawater electrolytes. Impressively, the performance of Fe–Ni/Ni₃S₂/NF electrode is also superior than several others that have been previously described (Table S2). Despite the complex contaminants in natural seawater, such as bacteria, microorganisms, and minute particles, the activity of Fe–Ni/Ni₃S₂/NF electrode in natural seawater shows only a slight decline compared to that in simulated seawater [15, 44].

A two-electrode electrolyzer was constructed, pairing the Fe–Ni/Ni₃S₂/NF electrode (anode) with a previously reported catalyst of P-NiMoO (cathode), and tested for

overall seawater splitting in simulated and natural seawater electrolytes [31]. Interestingly, the electrolyzer displays excellent activity in various electrolytes, as illustrated in Fig. 5c. At ambient temperature, the electrolyzer achieves current densities of 100, 400 and 800 mA·cm⁻² in 1 mol·L⁻¹ KOH at voltages of 1.62, 1.65 and 1.69 V, respectively, which are even lower than those of IrO₂||Pt/C [45, 46]. The activity in 1 mol·L⁻¹ KOH + 0.5 mol·L⁻¹ NaCl and 1 mol·L⁻¹ KOH + seawater electrolytes decrease slightly and still remains extremely outstanding when it is compared to that in 1 mol·L⁻¹ KOH electrolyte. To achieve a current density of 100 mA·cm⁻² in 1 mol·L⁻¹ KOH + 0.5 mol·L⁻¹ NaCl and 1 mol·L⁻¹ KOH + seawater, voltages of 1.65 and 1.69 V are required, respectively. Such performance is even better than that of many other electrolyzers in alkaline seawater

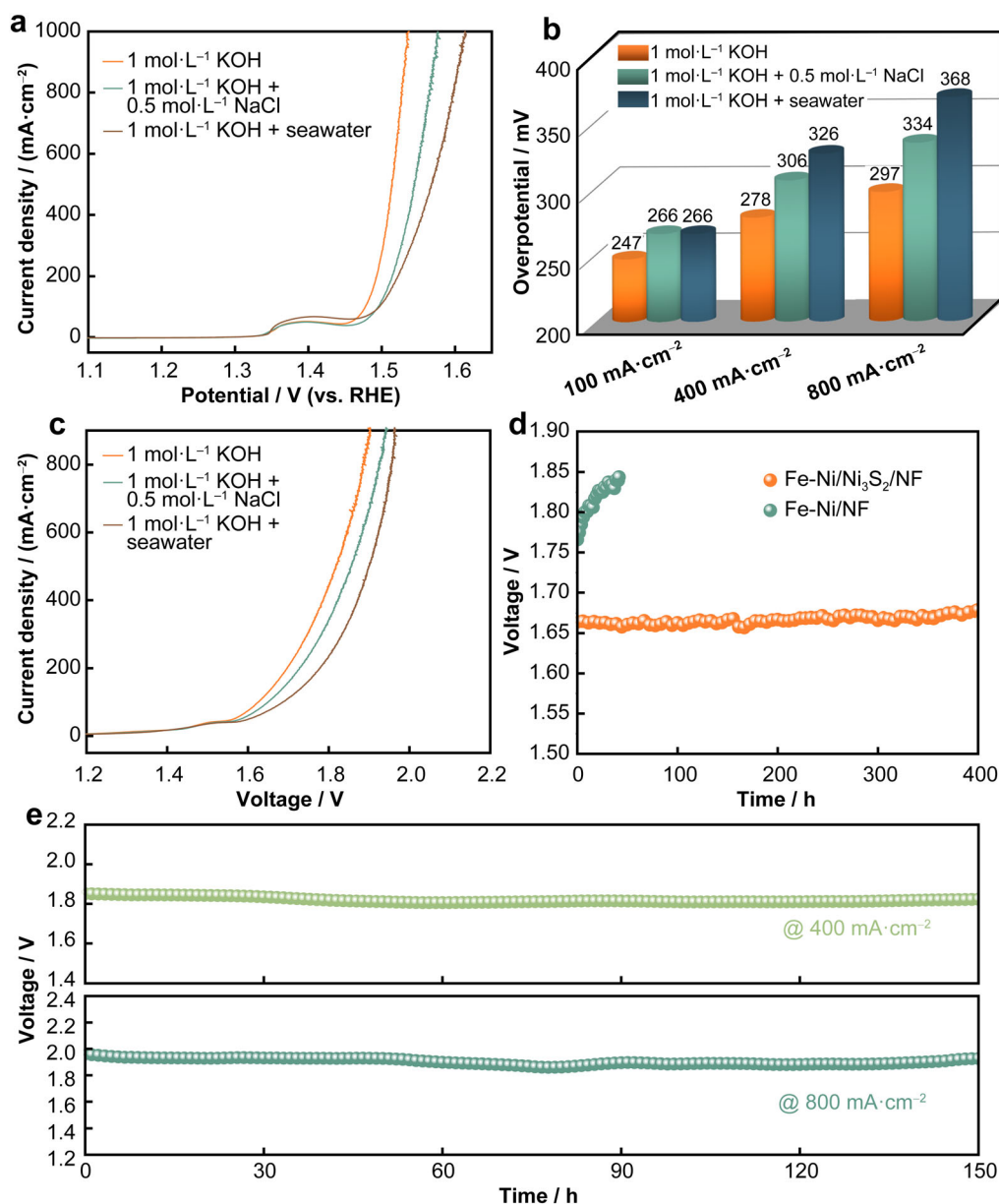


Fig. 5 **a** Polarization curves and **b** comparison of overpotentials required to achieve current densities of 100, 400 and 800 mA·cm⁻² of Fe-Ni/Ni₃S₂/NF electrode tested in different electrolytes; **c** overall seawater splitting polarization curves in different electrolytes; durability tests of electrolyzer at a constant current density of **d** 100 mA·cm⁻², **e** 400 mA·cm⁻² and 800 mA·cm⁻² in 1 mol·L⁻¹ KOH + seawater at 25 °C

(Table S3). Even at a high current density of 800 mA·cm⁻², the corresponding voltages in alkaline simulated and natural seawater are 1.92 and 1.95 V, respectively. Then, a gas collection device was used to determine the quantities of gaseous products generated over the electrolyzer in 1 mol·L⁻¹ KOH + seawater. As shown in Fig. S13, the measured quantities agree with the expected computations, and the Faradaic efficiency is around 100%, demonstrating high OER selectivity on the anode. The electrolyzer is also highly durable in alkaline natural seawater. The observed voltages in 1 mol·L⁻¹

KOH + seawater electrolyte remain remarkably stable at a constant current density of 100 mA·cm⁻² (Fig. 5d). To emphasize the significance of SO₄²⁻, another Fe-Ni/NF anode was fabricated without Ni₃S₂, and its morphology is shown in Fig. S14. According to Fig. S15a, in alkaline simulated seawater and natural seawater, the needed overpotentials to achieve a current density of 100 mA·cm⁻² are 330 and 380 mV, respectively. When pairing the Fe-Ni/NF anode with the P-NiMoO cathode, the two-electrode electrolyzer requires voltages of 1.85 and 1.87 V in 1 mol·L⁻¹ KOH + 0.5 mol·L⁻¹ NaCl and

1 mol·L⁻¹ KOH + seawater, respectively, to achieve a current density of 100 mA·cm⁻² (Fig. S15b). Unfortunately, the stability of Fe–Ni/NF||P–NiMoO system is extremely poor as evidenced by a sharp increase in voltage (Fig. 5d). The decrease in stability is primarily caused by the corrosion of Cl⁻ in seawater, proving that the presence of SO₄²⁻ in Fe–Ni/Ni₃S₂/NF electrode successfully alleviates chlorine corrosion and boosts stability. Its stability was subsequently investigated at high current densities of 400 and 800 mA·cm⁻² in 1 mol·L⁻¹ KOH + seawater electrolyte to meet industrial use. As shown in Fig. 5e, the voltage exhibits minimal increases after continuous operation for 150 h. The electrolyzer works well even at a higher current density of 800 mA·cm⁻², demonstrating its excellent potential for hydrogen production from seawater.

Raman spectrum in Fig. S16 is utilized to characterize the synthesized catalysts. The broad peak bands marked in blue are assigned to Ni₃S₂ [47, 48], while the bands at 460 and 540 cm⁻¹ are assigned to the stretching vibrations of FeNi (oxy)hydroxide [31]. During the OER process, the in-situ formed FeOOH/NiOOH interfaces in Fe–Ni/Ni₃S₂/NF electrode seem to serve as the main active material, which could be responsible for the improved catalytic performance [49]. Additionally, the intense peak at 982 cm⁻¹ is assigned to SO₄²⁻, which originates from the oxidation of Ni₃S₂ under a certain current density [14]. During the constant current test over an extended period, the inner layer of Ni₃S₂ will undergo continuous oxidation to produce SO₄²⁻. These SO₄²⁻ species aggregate on the surface of the active sites to form a passivating layer, which can mitigate the corrosion of Cl⁻ and enhance the stability of seawater splitting.

To investigate the morphology and structure of the catalyst after the long-term durability test, SEM, XRD and XPS analyses were performed. Figure S17 displays SEM images of the anodic Fe–Ni/Ni₃S₂/NF electrode after durability test in alkaline seawater. It can be seen that the overall nanoflower morphology remains intact, although some insoluble precipitates have formed. This result indicates that even when parts of the catalytic surface are coated by precipitates, the underlying or side regions of the nanoflower structure may still be in contact with the electrolyte, allowing seawater electrolysis to proceed. The special structure provides a large surface area to expose active sites, thereby greatly improving the activity of seawater splitting. As shown in Fig. S18, the XRD pattern still shows distinct peaks corresponding to NF and Ni₃S₂. In addition, XPS spectra were also measured to better confirm the structure of catalysts after OER. As displayed in Fig. S19a, new peaks appear at 856.3 and 874.3 eV, which are related to Ni³⁺ of NiOOH, further confirming the formation of NiOOH species after stability test. Fe 2p_{3/2} and Fe 2p_{1/2} are located at 711.8 and 724.5 eV, respectively

(Fig. S19b), nearly in the same positions as before the OER process. Besides, there are three peaks centered at 529.2, 531.1 and 532.4 eV detected in O 1s spectrum (Fig. S19c), which were ascribed to adsorbed H₂O, M–OH and M–O, respectively. Notably, the M–O peak becomes stronger due to the conversion of Ni₃S₂ or Ni(OH)₂ into NiOOH during the OER process. The S 2p spectrum, as shown in Fig. S19d, reveals the signals corresponding to Ni₃S₂ and SO₄²⁻ species. However, the intensities of the respective peaks are relatively low. This can be attributed to the continuous consumption and reconstruction of Ni₃S₂ during the catalytic reactions during OER.

4 Conclusion

In summary, a hierarchical Fe–Ni/Ni₃S₂/NF electrode has been constructed to enhance seawater splitting. The FeOOH/Ni(OH)₂ heterostructures possess large specific surface areas, providing a significant number of active sites, thereby contributing to the enhanced electrode activity. Furthermore, the inner Ni₃S₂ layer acts not only as a conductive interlayer but also as a sulfur source to form SO₄²⁻-rich passivation layers to alleviate Cl⁻ corrosion. Thus, the as-synthesized Fe–Ni/Ni₃S₂/NF electrode exhibited excellent catalytic activity, requiring only an overpotential of 266 mV at 100 mA·cm⁻² in 1 mol·L⁻¹ KOH + seawater electrolyte. The two-electrode electrolyzer, consisting of this anode and the previously reported cathode, requires a low voltage of 1.69 V at a current density of 100 mA·cm⁻² in alkaline seawater at 25 °C and exhibits high stability for 400 h. Overall, the catalysts exhibit high activity and stability, suggesting a high potential for fast hydrogen production in seawater electrolysis.

Acknowledgements This study was financially supported by the National Natural Science Foundation of Shandong Province (Nos. ZR2022QB062 and ZR2021MB070), the DNL Cooperation Fund (No. DNL202010), Research Innovation Fund (No. QIBEBTSZ201801), and the DICP and QIBEBT (No. UN201804).

Declarations

Conflict of interests The authors declare that they have no conflict of interest.

References

- [1] Ren XZ, Li XH, Peng YJ, Wang GJ, Yin J, Zhao XC, Wang W, Wang XB. FeNiS₂/reduced graphene oxide electrocatalysis with reconstruction to generate FeNi oxo/hydroxide as a highly-efficient water oxidation electrocatalyst. *Rare Met.* 2022;41(12): 4127. <https://doi.org/10.1007/s12598-022-02104-z>.



- [2] Carley S, Konisky DM. The justice and equity implications of the clean energy transition. *Nat Energy*. 2020;5(8):569. <https://doi.org/10.1038/s41560-020-0641-6>.
- [3] Guo X, Wan X, Liu QT, Li YC, Li WW, Shui JL. Phosphated IrMo bimetallic cluster for efficient hydrogen evolution reaction. *eScience*. 2022;2(3):304. <https://doi.org/10.1016/j.esci.2022.04.002>.
- [4] Sun ZX, Sun LJ, Koh SW, Ge JY, Fei JP, Yao MQ, Hong W, Liu SD, Yamauchi Y, Li H. Photovoltaic-powered supercapacitors for driving overall water splitting: a dual-modulated 3d architecture. *Carbon Energy*. 2022;4(6):1262. <https://doi.org/10.1002/cey2.213>.
- [5] Xie XH, Song M, Wang LG, Engelhard MH, Luo LL, Miller A, Zhang YY, Du L, Pan HL, Nie ZM, Chu YY, Estevez L, Wei ZD, Liu H, Wang CM, Li DS, Shao YY. Electrocatalytic hydrogen evolution in neutral pH solutions: dual-phase synergy. *ACS Catal*. 2019;9(9):8712. <https://doi.org/10.1021/acscatal.9b02609>.
- [6] Fan C, Jiang X, Chen JY, Wang X, Qian SY, Zhao CZ, Ding LF, Sun DM, Tang YW. Low-load Pt nanoclusters anchored on graphene hollow spheres for efficient hydrogen evolution. *Small Struct*. 2021;2(1):2000017. <https://doi.org/10.1002/ssr.202000017>.
- [7] Reier T, Nong HN, Teschner D, Schlögl R, Strasser P. Electrocatalytic oxygen evolution reaction in acidic environments—reaction mechanisms and catalysts. *Adv Energy Mater*. 2017;7(1):1601275. <https://doi.org/10.1002/aenm.201601275>.
- [8] Li JX, Wang SL, Chang JF, Feng LG. A review of Ni based powder catalyst for urea oxidation in assisting water splitting reaction. *Adv Powder Mater*. 2022;1(3):100030. <https://doi.org/10.1016/j.apmate.2022.01.003>.
- [9] Li ZJ, Wu XD, Jiang X, Shen BB, Teng ZS, Sun DM, Fu GT, Tang YW. Surface carbon layer controllable Ni₃Fe particles confined in hierarchical N-doped carbon framework boosting oxygen evolution reaction. *Adv Powder Mater*. 2022;1(2):100020. <https://doi.org/10.1016/j.apmate.2021.11.007>.
- [10] Dresp S, Dionigi F, Klingenhof M, Strasser P. Direct electrolytic splitting of seawater: opportunities and challenges. *ACS Energy Lett*. 2019;4(4):933. <https://doi.org/10.1021/acseenergylett.9b00220>.
- [11] Dresp S, Thanh TN, Klingenhof M, Brückner S, Hauke P, Strasser P. Efficient direct seawater electrolyzers using selective alkaline NiFe-LDH as OER catalyst in asymmetric electrolyte feeds. *Energy Environ Sci*. 2020;13(6):1725. <https://doi.org/10.1039/D0EE01125H>.
- [12] Keane TP, Nocera DG. Selective production of oxygen from seawater by oxidic metallate catalysts. *ACS Omega*. 2019;4(7):12860. <https://doi.org/10.1021/acsomega.9b01751>.
- [13] Yu L, Wu LB, McElhenny B, Song SW, Luo D, Zhang FH, Yu Y, Chen S, Ren ZF. Ultrafast room-temperature synthesis of porous S-doped Ni/Fe (oxy)hydroxide electrodes for oxygen evolution catalysis in seawater splitting. *Energy Environ Sci*. 2020;13(10):3439. <https://doi.org/10.1039/D0EE00921K>.
- [14] Kuang Y, Kenney MJ, Meng YT, Hung WH, Liu YJ, Huang JE, Prasanna R, Li PS, Li YP, Wang L, Lin MC, McGehee MD, Sun XM, Dai HJ. Solar-driven, highly sustained splitting of seawater into hydrogen and oxygen fuels. *Proc Natl Acad Sci*. 2019;116(14):6624. <https://doi.org/10.1073/pnas.1900556116>.
- [15] Tong WM, Forster M, Dionigi F, Dresp S, Sadeghi Erami R, Strasser P, Cowan AJ, Farràs P. Electrolysis of low-grade and saline surface water. *Nat Energy*. 2020;5(5):367. <https://doi.org/10.1038/s41560-020-0550-8>.
- [16] Dionigi F, Reier T, Pawolek Z, Glied M, Strasser P. Design criteria, operating conditions, and nickel–iron hydroxide catalyst materials for selective seawater electrolysis. *Chemsuschem*. 2016;9(9):962. <https://doi.org/10.1002/cssc.201501581>.
- [17] Okada T, Abe H, Murakami A, Shimizu T, Fujii K, Wakabayashi T, Nakayama M. A bilayer structure composed of Mg/Co-MnO₂ deposited on a Co(OH)₂ film to realize selective oxygen evolution from chloride-containing water. *Langmuir*. 2020;36(19):5227. <https://doi.org/10.1021/acs.langmuir.0c00547>.
- [18] Vos JG, Wezendonk TA, Jeremiasse AW, Koper MT. MnO_x/IrO_x as selective oxygen evolution electrocatalyst in acidic chloride solution. *J Am Chem Soc*. 2018;140(32):10270. <https://doi.org/10.1021/jacs.8b05382>.
- [19] Zhao YQ, Jin B, Zheng Y, Jin HY, Jiao Y, Qiao SZ. Charge state manipulation of cobalt selenide catalyst for overall seawater electrolysis. *Adv Energy Mater*. 2018;8(29):1801926. <https://doi.org/10.1002/aenm.201801926>.
- [20] Liang CW, Zou PC, Nairan A, Zhang YQ, Liu JX, Liu KW, Hu SY, Kang FY, Fan HJ, Yang C. Exceptional performance of hierarchical Ni-Fe oxyhydroxide@NiFe alloy nanowire array electrocatalysts for large current density water splitting. *Energy Environ Sci*. 2020;13(1):86. <https://doi.org/10.1039/C9EE02388G>.
- [21] Niu S, Jiang WJ, Tang T, Yuan LP, Luo H, Hu JS. Autogenous growth of hierarchical NiFe(OH)_x/FeS nanosheet-on-microsheet arrays for synergistically enhanced high-output water oxidation. *Adv Funct Mater*. 2019;29(36):1902180. <https://doi.org/10.1002/adfm.201902180>.
- [22] Wang W, Wang ZX, Hu YC, Liu YC, Chen SL. A potential-driven switch of activity promotion mode for the oxygen evolution reaction at Co₃O₄/NiO_x/H₂ interface. *eScience*. 2022;2(4):438. <https://doi.org/10.1016/j.esci.2022.04.004>.
- [23] Huang HJ, Wang YL, Li MH, Yang H, Chen ZH, Jiang Y, Ye SF, Yang YX, He SN, Pan HG, Wu XJ, Yao Y, Gu M, Yu Y. Optimizing the Fermi level of a 3D current collector with Ni₃S₂/Ni₃P heterostructure for dendrite-free sodium-metal batteries. *Adv Mater*. 2023;35(17):2210826. <https://doi.org/10.1002/adma.202210826>.
- [24] Li M, Pan XC, Jiang MQ, Zhang YF, Tang YW, Fu GT. Interface engineering of oxygen-vacancy-rich CoP/CeO₂ heterostructure boosts oxygen evolution reaction. *Chem Engin J*. 2020;395:125160. <https://doi.org/10.1016/j.cej.2020.125160>.
- [25] Jin HY, Liu X, Vasileff A, Jiao Y, Zhao YQ, Zheng Y, Qiao SZ. Single-crystal nitrogen-rich two-dimensional Mo₅N₆ nanosheets for efficient and stable seawater splitting. *ACS Nano*. 2018;12(12):12761. <https://doi.org/10.1021/acsnano.8b07841>.
- [26] Juodkazytė J, Šebeka B, Savickaja I, Petrulevičienė M, Butkutė S, Jasulaitienė V, Selskis A, Ramanauskas R. Electrolytic splitting of saline water: durable nickel oxide anode for selective oxygen evolution. *Int J Hydrogen Energy*. 2019;44(12):5929. <https://doi.org/10.1016/j.ijhydene.2019.01.120>.
- [27] Kato Z, Sato M, Sasaki Y, Izumiya K, Kumagai N, Hashimoto K. Electrochemical characterization of degradation of oxygen evolution anode for seawater electrolysis. *Electrochim Acta*. 2014;116:152. <https://doi.org/10.1016/j.electacta.2013.10.014>.
- [28] Huang WH, Lin CY. Iron phosphate modified calcium iron oxide as an efficient and robust catalyst in electrocatalyzing oxygen evolution from seawater. *Faraday Discuss*. 2019;215:205. <https://doi.org/10.1039/C8FD00172C>.
- [29] Song HJ, Yoon H, Ju B, Lee DY, Kim D-W. Electrocatalytic selective oxygen evolution of carbon-coated Na₂Co_{1-x}Fe_xP₂O₇ nanoparticles for alkaline seawater electrolysis. *ACS Catal*. 2019;10(1):702. <https://doi.org/10.1021/acscatal.9b04231>.
- [30] Zhao YQ, Jin B, Vasileff A, Jiao Y, Qiao SZ. Interfacial nickel nitride/sulfide as a bifunctional electrode for highly efficient overall water/seawater electrolysis. *J Mater Chem A*. 2019;7(14):8117. <https://doi.org/10.1039/C9TA01903K>.
- [31] Yang C, Gao NN, Wang XL, Lu JJ, Cao LJ, Li YD, Liang HP. Stable and efficient seawater splitting on a porous phosphate-intercalated NiFe (oxy)hydroxide@NiMoO₄ core-shell



- micropillar electrode. *Energy Mater.* 2021;1:100015. <https://doi.org/10.20517/energymater.2021.16>.
- [32] Xu HB, Fei B, Cai GH, Ha Y, Liu J, Jia HX, Zhang JC, Liu M, Wu RB. Boronization-induced ultrathin 2D nanosheets with abundant crystalline-amorphous phase boundary supported on nickel foam toward efficient water splitting. *Adv Energy Mater.* 2020;10(3):1902714. <https://doi.org/10.1002/aenm.201902714>.
- [33] Feng XT, Jiao QZ, Zhang JT, Cui HR, Li HS, Zhao Y, Feng CH. Integrating amorphous molybdenum sulfide nanosheets with a $\text{Co}_9\text{S}_8/\text{Ni}_3\text{S}_2$ array as an efficient electrocatalyst for overall water splitting. *Langmuir.* 2022;38(11):3469. <https://doi.org/10.1021/acs.langmuir.1c03264>.
- [34] Li X, Yan KL, Rao Y, Dong B, Shang X, Han GQ, Chi JQ, Hu WH, Liu YR, Chai YM. Electrochemically activated NiSe- Ni_3S_2 hybrid nanorods as efficient electrocatalysts for oxygen evolution reaction. *Electrochim Acta.* 2016;220:536. <https://doi.org/10.1016/j.electacta.2016.10.138>.
- [35] Li S, Xi C, Jin YZ, Wu D, Wang JQ, Liu T, Wang H-B, Dong CK, Liu H, Kulinich SA. Ir-O-V catalytic group in Ir-doped $\text{NiV}(\text{OH})_2$ for overall water splitting. *ACS Energy Lett.* 2019;4(8):1823. <https://doi.org/10.1021/acseenergylett.9b01252>.
- [36] Wu YJ, Yang J, Tu TX, Li WQ, Zhang PF, Zhou Y, Li JF, Li JT, Sun SG. Evolution of cationic vacancy defects: a motif for surface restructuring of OER precatalyst. *Angew Chem Int Ed.* 2021;60(51):26829. <https://doi.org/10.1002/anie.202112447>.
- [37] Li CF, Xie LJ, Zhao JW, Gu LF, Tang HB, Zheng LR, Li GR. Interfacial Fe-O-Ni-O-Fe bonding regulates the active Ni sites of Ni-MOFs via iron doping and decorating with FeOOH for super-efficient oxygen evolution. *Angew Chem Int Ed.* 2022;61(17): e202116934. <https://doi.org/10.1002/anie.202116934>.
- [38] Zhou HQ, Yu F, Sun JY, He R, Chen S, Chu CW, Ren ZF. Highly active catalyst derived from a 3D foam of $\text{Fe}(\text{PO}_3)_2/\text{Ni}_2\text{P}$ for extremely efficient water oxidation. *Proc Natl Acad Sci U S A.* 2017;114(22):5607. <https://doi.org/10.1073/pnas.1701562114>.
- [39] Mitchell CE, Santos-Carballal D, Beale AM, Jones W, Morgan DJ, Sankar M, De Leeuw NH. The role of surface oxidation and Fe-Ni synergy in Fe-Ni-S catalysts for CO_2 hydrogenation. *Faraday Discuss.* 2021;230:30. <https://doi.org/10.1039/d0fd00137f>.
- [40] Wang HY, Chen LY, Tan L, Liu X, Wen YH, Hou WG, Zhan TR. Electrodeposition of NiFe-layered double hydroxide layer on sulfur-modified nickel molybdate nanorods for highly efficient seawater splitting. *J Colloid Interface Sci.* 2022;613:349. <https://doi.org/10.1016/j.jcis.2022.01.044>.
- [41] Yan D, Xiao SH, Li XY, Jiang JX, He QY, Li HC, Qin JQ, Wu R, Niu XB, Chen JS. NiS_2/FeS heterostructured nanoflowers for high-performance sodium storage. *Energy Mater Adv.* 2023;4: 0012. <https://doi.org/10.34133/energymatadv.0012>.
- [42] Wang P, Luo YZ, Zhang GX, Chen ZS, Ranganathan H, Sun SH, Shi ZC. Interface engineering of $\text{Ni}_x\text{S}_y/\text{MnO}_x\text{H}_y$ nanorods to efficiently enhance overall-water-splitting activity and stability. *Nano-micro Lett.* 2022;14(1):1. <https://doi.org/10.1007/s40820-022-00860-2>.
- [43] Yu XX, Yu ZY, Zhang XL, Zheng YR, Duan Y, Gao Q, Wu R, Sun B, Gao MR, Wang GX, Yu SH. “Superaerophobic” nickel phosphide nanoarray catalyst for efficient hydrogen evolution at ultrahigh current densities. *J Am Chem Soc.* 2019;141(18):7537. <https://doi.org/10.1021/jacs.9b02527>.
- [44] Wang SH, Yang P, Sun XF, Xing HL, Hu J, Chen P, Cui ZT, Zhu WK, Ma ZJ. Synthesis of 3D heterostructure Co-doped Fe_2P electrocatalyst for overall seawater electrolysis. *Appl Catal B-Environ.* 2021;297:120386. <https://doi.org/10.1016/j.apcatb.2021.120386>.
- [45] Yu L, Zhou HQ, Sun JY, Qin F, Yu F, Bao JM, Yu Y, Chen S, Ren ZF. Cu nanowires shelled with NiFe layered double hydroxide nanosheets as bifunctional electrocatalysts for overall water splitting. *Energy Environ Sci.* 2017;10(8):1820. <https://doi.org/10.1039/C7EE01571B>.
- [46] Hui L, Xue YR, Huang BL, Yu HD, Zhang C, Zhang DY, Jia DZ, Zhao YJ, Liu HB, Li YL. Overall water splitting by graphdiyne-exfoliated and-sandwiched layered double-hydroxide nanosheet arrays. *Nat Commun.* 2018;9(1):1. <https://doi.org/10.1038/s41467-018-07790-x>.
- [47] Huang SC, Meng YY, Cao YF, Yao F, He ZJ, Wang XX, Pan H, Wu MM. Amorphous NiWO_4 nanoparticles boosting the alkaline hydrogen evolution performance of Ni_3S_2 electrocatalysts. *Appl Catal B.* 2020;274:119120. <https://doi.org/10.1016/j.apcatb.2020.119120>.
- [48] Feng LL, Yu GT, Wu YY, Li GD, Li H, Sun YH, Asefa T, Chen W, Zou XX. High-index faceted Ni_3S_2 nanosheet arrays as highly active and ultrastable electrocatalysts for water splitting. *J Am Chem Soc.* 2015;137(44):14023. <https://doi.org/10.1021/jacs.5b08186>.
- [49] Yan P, Liu Q, Zhang H, Qiu LC, Wu HB, Yu XY. Deeply reconstructed hierarchical and defective $\text{NiOOH}/\text{FeOOH}$ nanoboxes with accelerated kinetics for the oxygen evolution reaction. *J Mater Chem A.* 2021;9(28):15586. <https://doi.org/10.1039/D1TA03362J>.

Springer Nature or its licensor (e.g. a society or other partner) holds exclusive rights to this article under a publishing agreement with the author(s) or other rightsholder(s); author self-archiving of the accepted manuscript version of this article is solely governed by the terms of such publishing agreement and applicable law.